

Manufacturing Tolerance Effects on Ship Rudder Performance

John P. Hackett

Northrop Grumman Ship Systems

Wesley H. Brewer

Computational Simulation and Design Center, Mississippi State University

Manufacturing tolerances can affect ship rudder lift, drag, torque, cavitation, and surface erosion. Computational fluid dynamics (CFD) is used in this study to evaluate the effects of manufacturing variations from an ideal design. We used CFD to analyze four different types of variations: (1) leading-edge droop, (2) trailing-edge twist, (3) spanwise twist, and (4) longitudinal misalignment. We examined the effects of variations on a typical navy-type spade rudder, using the CFD code Unstructured, Unsteady Computation of Field Equations (U²NCLE) in the numerical simulation.

The resulting computations for the deformed rudders reveal that construction variations that cause trailing-edge twist have the greatest effect on rudder performance, with a lift performance deficit of 4% for a 0.2% construction variation. More significant, the numerical investigation shows that, despite a negligible effect on lift and drag, geometric variations related to trailing-edge twist can strongly affect rudder torque performance. All other manufacturing variations result in less than a 0.5% performance deficit for the same 0.2% construction variation, although further analysis is needed to determine the effect of spanwise twist on ship maneuverability. Those findings indicate that the construction tolerances associated with leading-edge droop and longitudinal misalignment can be loosened, spanwise-twist tolerances should be maintained pending further analysis, and tolerances associated with trailing-edge twist should be maintained.

Introduction

Modern naval vessels are typically outfitted with twin rudders located behind the ship's propellers. Twin rudders provide superior maneuverability and redundancy. Placement of the rudders in the propeller wash increases the effectiveness of the rudders at low vessel speed. Modern naval rudders consist of a skeletal structure of ribs, stringers, and castings, assembled and covered with notch-tough steel plating, creating a streamlined foil body, as shown in Figure 1. The leading-edge and trailing-edge elements are typically castings connected chordwise by plate ribs, which in turn are connected spanwise by stringers and leading- and trailing-edge castings. The use of heat-treated steels, along with the size, thickness, and weight of components, requires different manufacturing techniques. All of these factors in turn necessitate significant care during assembly to ensure that the final product meets all imposed tolerances. Rudders fabricated by Northrop Grumman Ship Systems are large structures. A typical rudder may have a midspan chord c of 18 ft and a span of 20 ft. Because of their size, rudders are assembled outdoors. Maintaining strict rudder tolerances will keep the cost of rudder fabrication high.

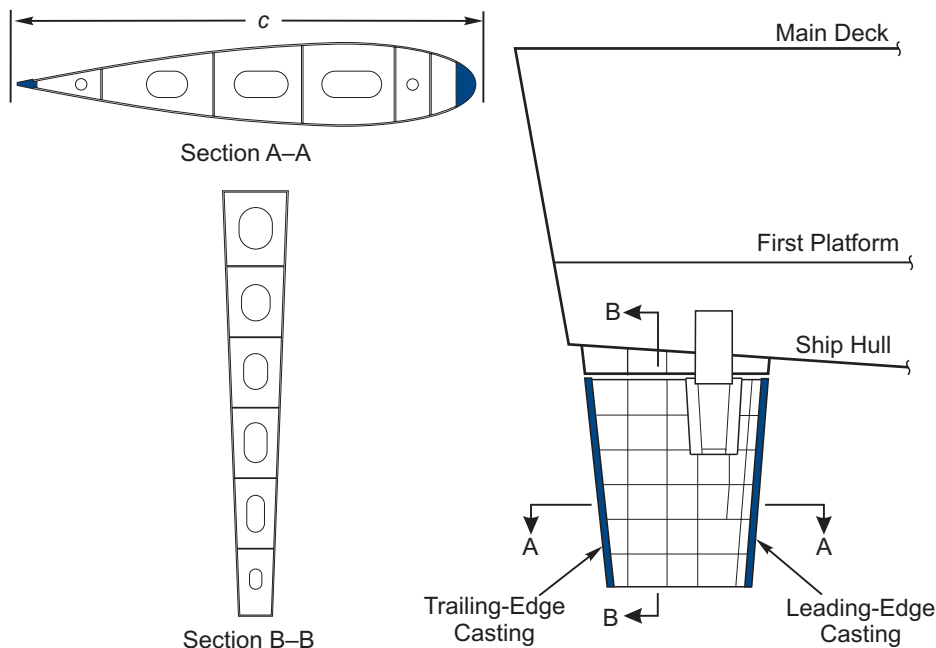


Figure 1. Modern naval rudder structure

Naval architects size the steering gear based on the ideal performance of the rudder. Excessive deviation from the ideal dimensions of the rudder during construction can produce excessive steering gear torques while the ship is maneuvering. Such torques would probably be asymmetric, requiring more force to turn the rudder either inward or outward.

Hydrodynamic torques are a concern not only because of the magnitude of the force the steering gear must produce, but also because of their effects on the rudder azimuthing rate, which is typically designated in the ship’s specifications. Hydrodynamic torques can drive the size of the steering gear. Likewise, deformations can lead to premature cavitation of the rudder, which may affect the ship’s signature and possibly lead to rudder erosion, requiring premature rudder structural renewal.

The origins of the current tight rudder construction tolerances go back to the days when iron and steel ships were first introduced into service. Ship designers of that era agreed that rudder geometry was critical. Not until computers became a design tool was it possible to perform simplified potential flow (ideal fluid) computations. Our naval architect predecessors had to evaluate performance degradation due to construction tolerance variations using only full-scale trials or subscale model tests in either water or air:

- *Full-scale trials* are very expensive, requiring a ship to be pulled out of service, dry-docked several times for instrumenting and changing out rudders with different built-in deformities, and then performance-tested at sea, with all the complications that brings (e.g., weather and sea conditions, time constraints, water depth, presence of other traffic).
- *Subscale model tests* have, in the past, investigated large variations in rudder shape and geometry. However, such tests are problematic because of the very nature of the scale factor of the model and the size of any prototype construction deformations. The magnitude of the scale tolerance is difficult to replicate on a subscale model. In addition, in model tests, it is difficult to match full-scale Reynolds numbers.

The research presented here is an attempt to use modern digital computers and a viscous flow solver to take a rational look at the effect of rudder construction tolerance variations on the performance of the rudder. Recent advances in computational fluid dynamics (CFD) enable naval architects to address those issues very precisely and at a full-scale Reynolds number. Thus, CFD can give highly accurate information regarding the differences in performance between the specified design (ideal rudder) and the as-built rudder with construction tolerances consumed, resulting in cost savings during construction.

In this study, Mississippi State University's unstructured flow solver, Unstructured, Unsteady Computation of Field Equations (U²NCLE), was used to evaluate performance variations of prescribed rudder tolerances. U²NCLE solves the Reynolds-averaged Navier-Stokes (RANS) equations interactively with a two-equation turbulence model. We examined the effects of four different manufacturing variations on a nominal LHD amphibious assault ship's rudder: leading-edge droop, trailing-edge twist, spanwise twist, and longitudinal misalignment. As with most complicated technical problems, simplifying assumptions were made:

- The performance of the ship making critical maneuvers is directly related to the amount of lift the rudder creates at an angle of attack (AOA). A significant degradation of the rudder's performance will reduce the ship's maneuverability.
- The problem is further simplified by removing the rudder from the hull wake and propeller race and placing it in a uniform flow field. The rudders on the LHD are located under the hull of the ship and are not exposed to the free surface. Therefore, a rigid wall replaces the hull of the ship.
- The number of possible rudder deformations from the ideal rudder shape was limited to those that by inspection may have the greatest influence on rudder performance.
- Each deformation was investigated as if it were the only deformation present.

This paper first addresses the methodology used to generate the computational grids, perform the nonlinear flow analysis, and implement the parallel execution of the flow solver. Then the simplifying assumptions used in the calculations are discussed. Next, the code is validated, using published experimental data for a destroyer rudder [1]. Finally, the LHD rudder's performance with various construction deformations is analyzed and discussed.

Computational Modeling Methodology

This section presents the details of the entire computational modeling procedure. First, the computer-aided models are developed using computer-aided design (CAD) software. Next, grid-generation software is used to "nodalize" the flow domain (i.e., define millions of discrete points on and around the rudder, where the viscous-flow solution will be calculated). Finally, the flow solver is used on the RANS equations at each point in the grid. Parallel computing significantly reduces the time required to perform the simulations.

Geometric Modeling of Rudders. Mississippi State University's CAD modeling software, SolidMesh, was used to generate the computational grids that represent the rudder shape. The root section of the LHD rudder is a National Advisory Committee for Aeronautics (NACA) 0021 foil section and the tip an NACA 0009. The mathematical NACA sections have a razor-sharp trailing edge, which is not producible in the real shipbuilding world. Because the razor-sharp trailing edge may affect the CFD-computed performance of the rudder, the trailing-edge geometries were built with a truncation thickness of about 15/16 in. at the root and 5/16 in. at the tip to reflect fabrication. The truncated trailing edge

can be seen in the case-2 trailing-edge graph in Figure 2. The rudder has a span of 219 in. The midspan chord was used to nondimensionalize the computed force coefficients.

Table 1 presents the suite of four basic variations of rudder tolerances used in this study. Each variation case is subdivided into different subcases, and the characteristics of each subcase are specified.

The suite of four variations and their subdivisions are diagrammed in Figure 3. The variations in this figure are exaggerated to make them more plainly visible. Figure 2 shows graphical representations of the ideal and actual (deformed) rudders used in the computations. Case 4 (longitudinal misalignment) was excluded from Figure 2 because the actual variations are so slight, they are not visible in this graphic.

Grid Generation. CFD solves the Navier-Stokes equations at discrete locations in space. The definition of such discrete loci of points is typically called *grid generation*, or *nodalization*. The quality of the CFD results can vary significantly, depending on the quality of the grid points.

Grid generation is typically classified as either structured or unstructured. Each point in a structured grid is surrounded by four neighbor points. Structured grids can be divided into Cartesian grids or body-fitted grids, where the grid points are stretched about the geometry. Figure 4 shows examples of (a) a Cartesian structured grid, (b) a body-fitted

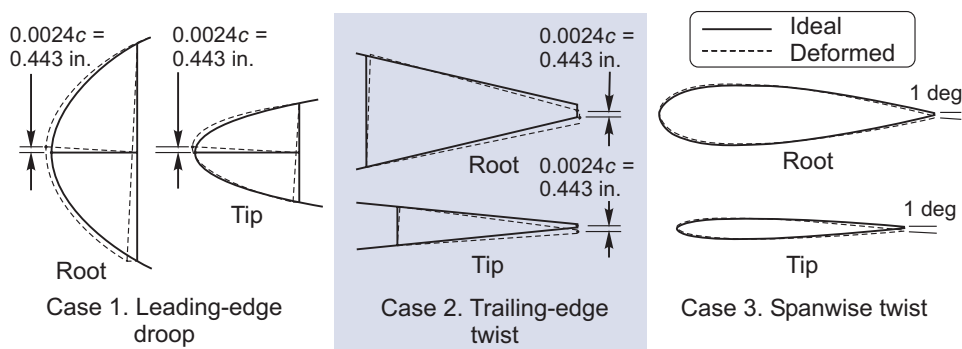


Figure 2. Ideal and actual rudder variations used in this study

Table 1. Specifications of suite of four rudder tolerance variations

Variation	Case	Specification
Leading-edge droop	1a	0.24% from <i>c</i> at root
	1b	0.24% from <i>c</i> at tip
	1c	0.24% from <i>c</i> at root and tip
Trailing-edge twist	2a	0.24% from <i>c</i> at root
	2b	0.24% from <i>c</i> at tip
	2c	0.24% from <i>c</i> at root and tip
Spanwise twist	3a	1 deg AOA at tip
	3b	1 deg AOA at root
Longitudinal misalignment	4a	0.23% <i>c</i> forward shift at midspan
	4b	0.23% <i>c</i> aft shift at midspan

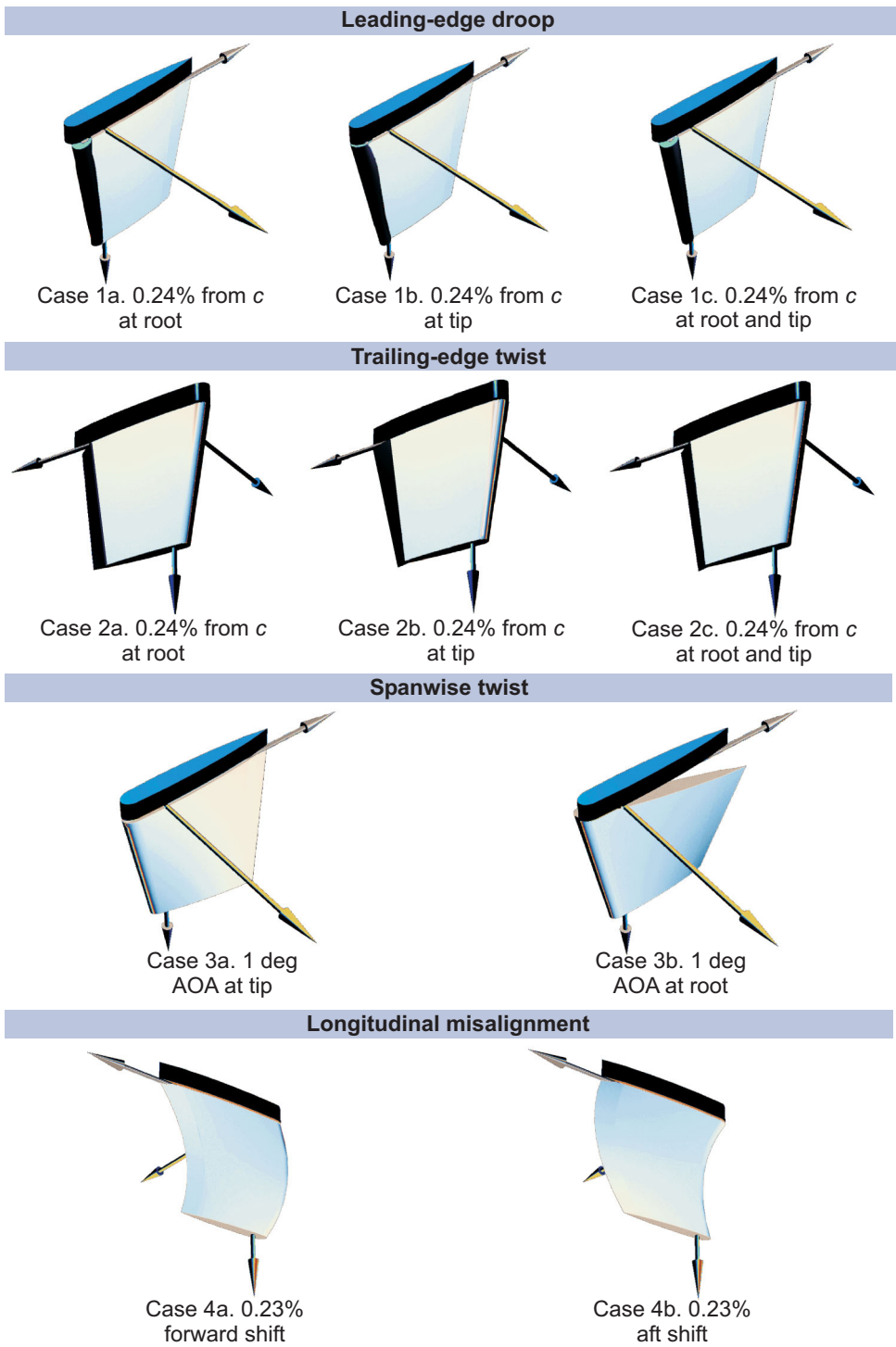


Figure 3. Diagrams of suite of four rudder tolerance variations, with variations exaggerated

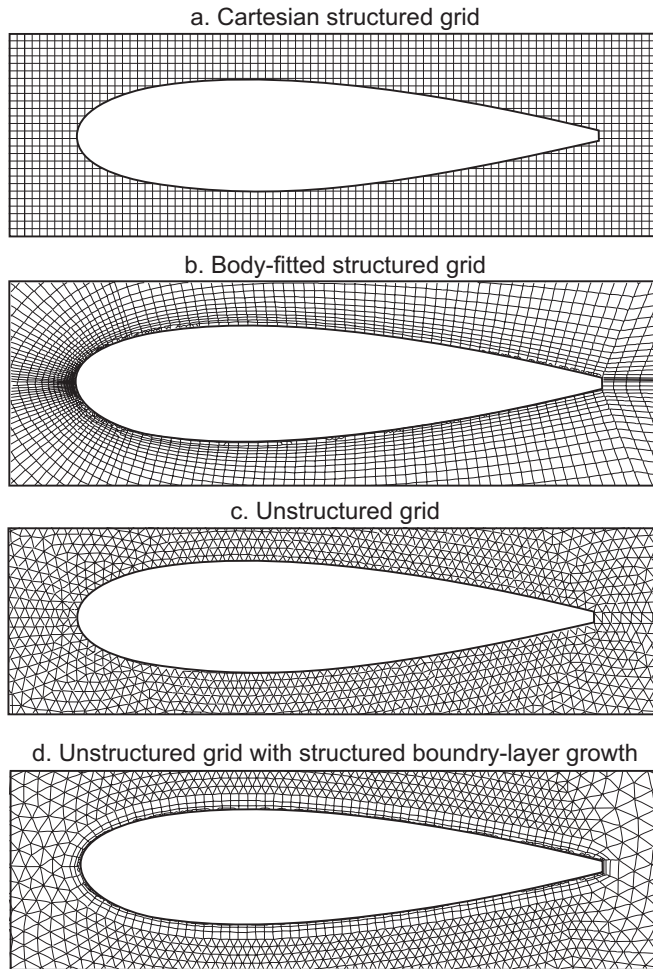


Figure 4. Evolution of grids for computational fluid dynamics as demonstrated on NACA 0021 foil section

structured grid, (c) an unstructured grid, and (d) an unstructured grid with structured boundary-layer growth for an NACA 0021 foil section. This study used the grid shown in Figure 4d. Note: The grids shown in Figure 4 illustrate the topology of the different grid types; however, the actual grids are significantly more dense.

Currently, the state-of-the-art approach is to use *unstructured* grids, where points need not have consistent neighbors and points can be arbitrarily added to any region of interest. Unstructured grids have two primary advantages over structured grids:

- The volume grids can be generated automatically (reducing grid-generation time from weeks or months for structured grids to less than a week for unstructured grids).
- Extremely complex geometries can be accommodated.

For RANS solutions, results of similar accuracy can be achieved for both structured and unstructured approaches.

In general, unstructured CFD incurs a much higher computational cost than structured grids, in both memory requirements and CPU time. On the other hand, unstructured grids

are much better suited for parallel processing, because the automated procedure can produce subgrids of virtually identical size to be run on each processor. Technically, that means the load-balancing efficiency is in general much higher for unstructured grids than for structured grids. (Typical values are 99% for unstructured, 80% for structured.) The unstructured approach also reorders the points to optimize for cache coherency.

Unstructured grids can be generated via either a Delaunay-triangulation or an advancing-front approach. This study uses an advancing-front technique, developed by Marcum and Weatherill [2], that “grows” the points from all boundary surfaces, as opposed to a simultaneous initial distribution of points in the volume.

Unstructured Grid Generation. Marcum and Weatherill [2] developed a very efficient local-reconnection procedure using advancing-front point placement and a combined Delaunay/min-max (minimize the maximum angle) type of local reconnection to generate triangular or tetrahedral element grids. Known as advancing front/local reconnection (AFLR), their approach differs substantially from earlier methods in that it implements a Delaunay/min-max reconnection criterion. In other words, it uses the existing grid as a search data structure for effective optimization of the three-dimensional tetrahedral element connectivity.

The grid generator works as follows: An initial grid is built using the AFLR techniques. Then a quality-improvement algorithm is executed that will insert additional points in areas where the tetrahedra have either very small minimum angles or excessively large maximum angles. The additional points are inserted by subdividing the current elements into smaller elements. Marcum has also extended the methodology for generation of high-aspect-ratio elements [3], right-angle elements [4], and solution-adapted grids [5].

High-quality grids have been generated about geometrically complex configurations using the same procedure. Results verify that, for isotropic grid generation, advancing-front point placement with a combined Delaunay/min-max connectivity criterion is the most efficient method for consistently producing the elements of highest quality [6].

RANS Numerical Solution

An efficient unstructured flow solver has been developed for simulations of three-dimensional unsteady compressible and incompressible high-Reynolds-number viscous flows about complete bodies, including appendages.

Unstructured Flow Solver. The numerical approach is to solve the three-dimensional time-dependent incompressible turbulent Navier-Stokes equations. They are solved using a finite-volume approach, wherein the integral form of the equations is discretized directly. The artificial compressibility idea of Chorin [7] is then introduced into the conservation-of-mass equation [8–10]. The use of artificial compressibility permits the experience gained in the numerical solution of compressible-flow problems to be exploited in the solution of incompressible-flow problems [2]. The nondimensional equations can be written in integral form as

$$\frac{\partial}{\partial t} \int_{\Omega} Q dV + \int_{\partial\Omega} \vec{F} \cdot \hat{n} dA = \frac{1}{Re} \int_{\partial\Omega} \vec{G} \cdot \hat{n} dA \quad , \quad (1)$$

where \hat{n} is the outward-pointing unit normal to the control volume Ω , A is the surface area of the control volumes, and other terms are defined in subsequent equations.

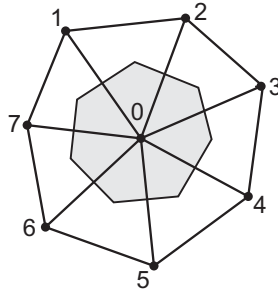


Figure 5. Typical dual-control volume

The finite-volume approach uses median dual-control volumes defined by the midpoints of each point-to-point edge, as well as the midpoint of the element volumes, as shown in Figure 5. There, node 0 is the center node, where the solution is being computed. To numerically integrate the convective flux terms in the governing equations, Gaussian quadrature is used over each control volume, where the midpoint of each edge is taken as the quadrature point. Mathematically, the convective flux term can be expressed as

$$\int_{\partial\Omega} \vec{F} \cdot \hat{n} dA \approx \sum_{i \in \mathbb{N}(0)} \vec{\Phi}_{0i} \cdot \vec{n}_{0i} \quad , \quad (2)$$

where the summation is performed around all surrounding nodes (e.g., nodes 1 through 7 in Figure 5).

In other words, the equations state that mass and momentum must be conserved for each finite-control volume. The vector of dependent variables and the components of the inviscid and viscous fluxes are given as

$$Q = \begin{bmatrix} P \\ u \\ v \\ w \end{bmatrix} \quad , \quad \vec{F} \cdot \hat{n} = \begin{bmatrix} \beta(\Theta - a_t) \\ u\Theta + \hat{n}_x P \\ v\Theta + \hat{n}_y P \\ w\Theta + \hat{n}_z P \end{bmatrix} \quad , \quad (3)$$

$$\vec{G} \cdot \hat{n} = \begin{bmatrix} 0 \\ \hat{n}_x \tau_{xx} + \hat{n}_y \tau_{xy} + \hat{n}_z \tau_{xz} \\ \hat{n}_x \tau_{yx} + \hat{n}_y \tau_{yy} + \hat{n}_z \tau_{yz} \\ \hat{n}_x \tau_{zx} + \hat{n}_y \tau_{zy} + \hat{n}_z \tau_{zz} \end{bmatrix} \quad , \quad (4)$$

where β is the artificial compressibility parameter, taken as 15 here; $u, v,$ and w are the components of the velocity vector corresponding to the $x, y,$ and z directions, respectively, besides being the components of the normalized control-volume face vector; and τ is defined in Equation (8). The velocity normal to a control-volume face Θ is defined as

$$\Theta = \hat{n}_x u + \hat{n}_y v + \hat{n}_z w + a_t \quad , \quad (5)$$

where the grid speed $a_t = -(u\hat{n}_x + v\hat{n}_y + w\hat{n}_z)$. This equation is used to define the velocity normal to the control-volume face. It is used in Equation (2), where $n_x, n_y,$ and n_z are the $x, y,$ and z components of the normal vector for the control surface of the control volume.

The variables in the preceding equations are nondimensionalized, using the midspan chord length c and free-stream values of density $\rho_\infty,$ velocity $U_\infty,$ and viscosity $\mu_\infty.$ Thus, the Reynolds number is defined as

$$Re = \frac{\rho_\infty U_\infty c}{\mu_\infty} \quad (6)$$

Pressure is normalized with

$$P = \frac{P^* - P_\infty}{\rho_\infty U_\infty^2} \quad (7)$$

where P^* is the local dimensional static pressure and P_∞ is the ambient pressure. The viscous stresses are

$$\tau_{ij} = (\mu + \mu_t) \left(\frac{\partial u_i}{\partial x_j} + \frac{\partial u_j}{\partial x_i} \right) \quad (8)$$

where μ and μ_t are the molecular and eddy viscosities, respectively; and $u_1 = u, u_2 = v, u_3 = w, x_1 = x, x_2 = y,$ and $x_3 = z.$

The basic solution algorithm is that of Anderson, Rausch, and Bonhaus [11]. To model turbulence, we can use either Coakley's two-equation $q-\omega$ turbulence model [12] or Spalart and Allmaras' one-equation model [13]. The discretized scheme uses a node-based finite-volume upwind approximation. The numerical flux for the inviscid part is evaluated with a second-order Roe scheme [14], whereas the viscous flux is evaluated with a finite-volume formulation that is equivalent to a Galerkin-type approximation (for a mesh consisting of tetrahedral elements only) or a directional-derivative, edge-based formulation (for a mesh with different element types). The time-advancement algorithm is based on the linearized backward-Euler time-difference scheme, which yields a linear system of equations for the solution at each time step. The Gauss-Seidel procedure is used to solve the linear system of equations at each time step.

The normal procedure for the solution of the discretized equations would be to linearize the spatial difference terms, move the terms not containing Δq^{n+1} to the right side of the equations [15], and solve for

$$\Delta q^{n+1} = q^{n+1} - q^n \quad (9)$$

where q is defined as

$$q = \int_{\Omega} Q dV \approx \bar{Q}V \quad (10)$$

where V is the volume of the local control volume. Such a solution procedure is particularly effective for problems expected to have steady-state solutions, because the sum of the spatial-difference operator terms, as well as q^{n+1} , would go to zero. For unsteady flow, however, the ideal situation would be to find q such that

$$\mathfrak{F}(q^{n+1}) = \frac{\Delta q_i^n}{\Delta t} + \mathfrak{R}(q^{n+1}) = 0 \quad . \quad (11)$$

That problem can be solved using Newton’s method [16], which for the function $\mathfrak{F}(x)$ would be

$$\begin{aligned} \mathfrak{F}'(q^{n+1,m})(q^{n+1,m+1} - q^{n+1,m}) = \\ \mathfrak{F}'(q^{n+1,m})\Delta q^{n+1,m} = -\mathfrak{F}(q^{n+1,m}) \quad , \end{aligned} \quad (12)$$

where $m = 1, 2, 3, \dots$ is the number of subiterations and $\mathfrak{F}'(x)$ is the Jacobian matrix of the vector $\mathfrak{F}(x)$. In principle, the generated sequence $q^{n+1,m+1}$ will converge to q^{n+1} and, hence, Equation (3) is satisfied.

A linear system of equations must be solved at each iteration of Newton’s method. For three-dimensional problems, a direct solution seems to be impractical [17]. In this study, we used symmetric Gauss-Seidel relaxation. For simplicity and because the flux Jacobian of the flux vector based on Roe’s formulation [14] is difficult to obtain analytically in three dimensions, the flux Jacobian $\partial\mathfrak{F}/\partial\bar{Q}$ is obtained approximately [17,18]. The fluxes are computed at the edge midpoints, according to the method of Roe:

$$F = 1/2 (F(Q_L) + F(Q_R)) - 1/2 (\tilde{A}^+ - \tilde{A}^-)(Q_R - Q_L) \quad , \quad (13)$$

$$\frac{\partial F}{\partial Q_L} \approx 1/2 (A(Q_L) + \tilde{A}^+ - \tilde{A}^-) = 1/2 (A(Q_L) + |\tilde{A}|) \quad , \quad (14)$$

$$\frac{\partial F}{\partial Q_R} \approx 1/2 (A(Q_R) - \tilde{A}^+ + \tilde{A}^-) = 1/2 (A(Q_R) - |\tilde{A}|) \quad , \quad (15)$$

where Q_L and Q_R are the solution values to the left and right of the edge midpoint.

The Roe dissipation matrix is

$$\tilde{A} = \tilde{R}\tilde{\Lambda}\tilde{R}^{-1} \quad , \quad (16)$$

where \sim represents a simple average between the left and right states, \tilde{A}^+ contains the positive eigenvalues $\tilde{\Lambda}^+$, and \tilde{A}^- contains the negative eigenvalues $\tilde{\Lambda}^-$, so that $\tilde{A} = \tilde{A}^+ - \tilde{A}^-$. \tilde{R} comprises the linearly independent right eigenvectors that come out of the decoupling of the Riemann problem, via the introduction of Roe-averaged variables [19]. \tilde{R} is constructed from the right eigenvectors of the flux Jacobian. The Roe-averaged matrix $|\tilde{A}|$ is averaged between left and right states and treated as constant in differentiation.

The solution scheme, known as discretized Newton relaxation [16] or the DNR scheme [17], is used in the unstructured flow solver to achieve an efficient solution. The resulting algorithm is known as Unsteady Computation of Field Equations (UNCLE). The unstructured flow solver, U²NCLE, uses the UNCLE algorithm to achieve an efficient solution.

Parallel Computing. Large-scale complex-flow simulations require enormous computer resources. Parallel computing can reduce the calendar time needed to run large cases by at least two or three orders of magnitude, as well as provide access to the substantial global memory required for highly complex problems. U²NCLE exploits coarse/medium-grained parallelism, using the single-program/multiple-data (SPMD) model, and employs the Message-Passing Interface (MPI) standard because of MPI's extensive portability and functionality. MPI defines standards for message-passing procedures on parallel clusters and supercomputers. It is implemented in several different software packages (e.g., MPICH and MPI/Pro).

The MPI/Pro implementation was used in this study. The parallel code solves the three-dimensional incompressible unsteady RANS equations using an implicit finite-volume approximation, with characteristic-based upwind flux approximations. The implicit approximation is solved at each time step using a Newton relaxation procedure analogous to that used in the sequential algorithm [18,20]. Domain decomposition is achieved using METIS, a software library for partitioning unstructured graphs. METIS reorders data structures to reduce the ordering of sparse matrices. The resulting partition map is used to distribute the data space onto a set of processors.

Static load balancing is performed during grid partitioning, taking into account available system resources. The time-linearized approximations at each time step are solved using a block-Jacobi symmetric Gauss-Seidel relaxation procedure that involves a point-to-point message exchange at each subiteration level.

Force Computations. U²NCLE computes lift, drag, and torque on the rudder by integrating the pressure and shear stresses over the entire rudder. The computed forces reported here are nondimensionalized as follows:

Lift coefficient C_L :

$$C_L = \frac{L}{1/2 \rho U^2 S} \quad , \quad (17)$$

Drag coefficient C_D :

$$C_D = \frac{D}{1/2 \rho U^2 S} \quad , \quad (18)$$

Torque coefficient C_Q :

$$C_Q = \frac{M_z}{1/2 \rho U^2 S c} \quad , \quad (19)$$

where L is the dimensional lift, D is the dimensional drag, M_z is the computed moment about the z -axis, ρ is the density, U is the velocity, and $S = 40,466 \text{ in.}^2$ is the projected profile area, equal to the 184.78-in. midspan chord length $c \times$ the 219-in. span.

Simulation Conditions. U²NCLE offers more than 90 input options, which allow for different types of turbulence models, different limiters, different solution algorithms, etc. Past experience has helped to narrow the right combination of options. Some options can affect performance significantly, whereas others mainly affect run time. Much initial work was performed in this study to determine the simulation conditions most suitable for such a problem:

- A two-equation $q-\omega$ turbulence model was used.
- A limiter was not used in the solution process.

- The flux Jacobians were approximated, rather than solved numerically or analytically.
- A symmetric Gauss-Seidel method was used to solve the resulting linearized system of equations.
- A Courant number of 200 was used.

Those conditions provided for a converged solution in five hours, using eight parallel processors.

Force Validation Study. A force validation study was performed to assess the validity of the U²NCLE method of computing forces correctly. The DDG 51 guided missile destroyer rudder is very similar to the LHD rudder, having an NACA 0023 root section and an NACA 0013 tip section. Shen et al. [1] performed model testing of the DDG 51 rudder in a 24-in. water tunnel at the David Taylor Model Basin. Those experiments were performed at a Reynolds number of one million.

Figure 6 shows the results of this study. Figure 6a shows excellent agreement between the lift coefficient computations and the experiment at $Re = 1.02 \times 10^6$. The turbulence model can even predict stall accurately. The experiment has a slight asymmetry, but the computation is symmetric about the angle of attack. Extending the computations to full scale introduced additional problems. At the full-scale Reynolds number ($Re = 2.2 \times 10^7$), one should expect a higher stall angle. However, the computations predict a lower stall angle

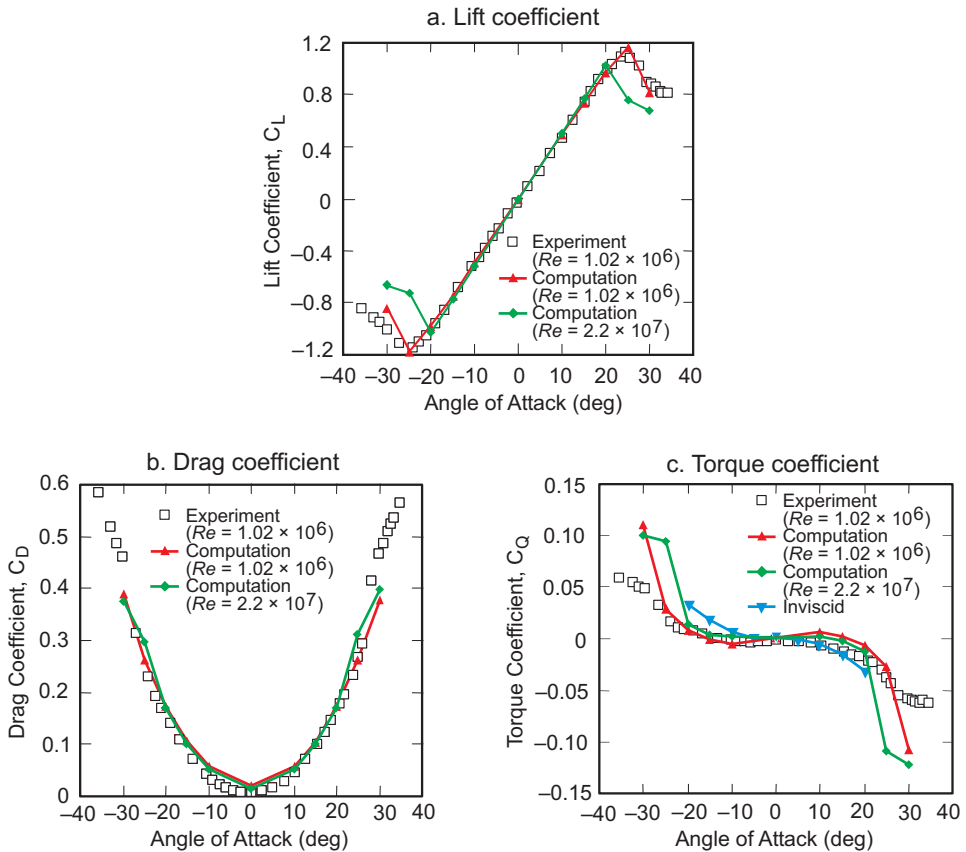


Figure 6. DDG 51 force validation results for lift, drag, and torque coefficients

of about 20 deg, which is physically incorrect. That underprediction is most likely due to a breakdown of the turbulence models at full-scale Reynolds numbers. It has been evidenced in other full-scale simulations (e.g., the flat-plate validation study at full-scale Reynolds numbers by Brewer [21]).

Figure 6b compares the simulation and experiment results for the drag coefficient. Although the simulation shows very favorable agreement at higher angles of attack (10 to 20 deg), the drag is overpredicted at low angles of attack by as much as 20%. The overprediction of drag is most likely attributable to the difficulty of computing the skin friction coefficient correctly—a difficulty that may be due to the inability to accurately predict the laminar-to-turbulent transition location. At low angles of attack, the skin friction coefficient dominates the drag force; at high angles of attack, the form drag dominates. The details of the skin friction computation and the difficulties of making precise predictions are discussed by Brewer [21].

Figure 6c compares the simulation and experiment results for the torque coefficient, which is the most difficult force coefficient to compute correctly, because it is affected by the accuracy of both the lift and drag computations. At low angles of attack, a positive AOA is predicted to yield a positive torque. Such behavior is physically impossible, and that erroneous result is most likely attributable to the overprediction of the drag coefficient at low angles of attack. In this study, we are comparing the performance of the ideal rudder geometry with the performance of rudders that have relatively small variations in geometry from the ideal. Therefore, any computational bias errors, such as those just discussed, are assumed to cancel out.

Effects of Viscosity. The effects of viscosity were studied by neglecting the viscous terms in U^2 NCLE, which in essence causes Equation (1) to become the Euler equation. In this case, fully isotropic grids must be generated, which neglects the refined boundary-layer grid spacing. Figure 7 shows the effects of running U^2 NCLE with viscosity (RANS) and without the viscous terms (Euler). As expected, the inviscid lift coefficient is higher, the inviscid drag coefficient is lower, and the inviscid torque coefficient is higher than with viscosity present.

Results of Rudder Performance Evaluation

The results for leading-edge droop, trailing-edge twist, spanwise twist, and longitudinal alignment can be seen in Figures 8, 9, 10, and 11, respectively. The graphs on the left show the lift, drag, and torque coefficients at various angles of attack. The graphs on the right show the percentage variation, from the ideal rudder value, of lift, drag, and torque at various angles of attack. The smaller the percentage variation, the less significant is the influence of construction deviation on rudder performance. Figure 12 summarizes the mean effects on rudder performance for each type of construction deformation.

Leading-Edge Droop. Figure 8 presents the lift, drag, and torque effects of leading-edge droop. The data show that leading-edge droop has very little effect on rudder performance. The right-hand graph demonstrates that the leading-edge droop occurring at the tip actually improves the lift coefficient at high angles of attack. Therefore, looser manufacturing tolerances are recommended at the tip.

Trailing-Edge Twist. Figure 9 presents the effects of trailing-edge twist on rudder performance. For the lift coefficient, the effect of the twist is roughly equal at the root and at the tip. Therefore, when both the root and tip are twisted (case 2c), the effect is roughly

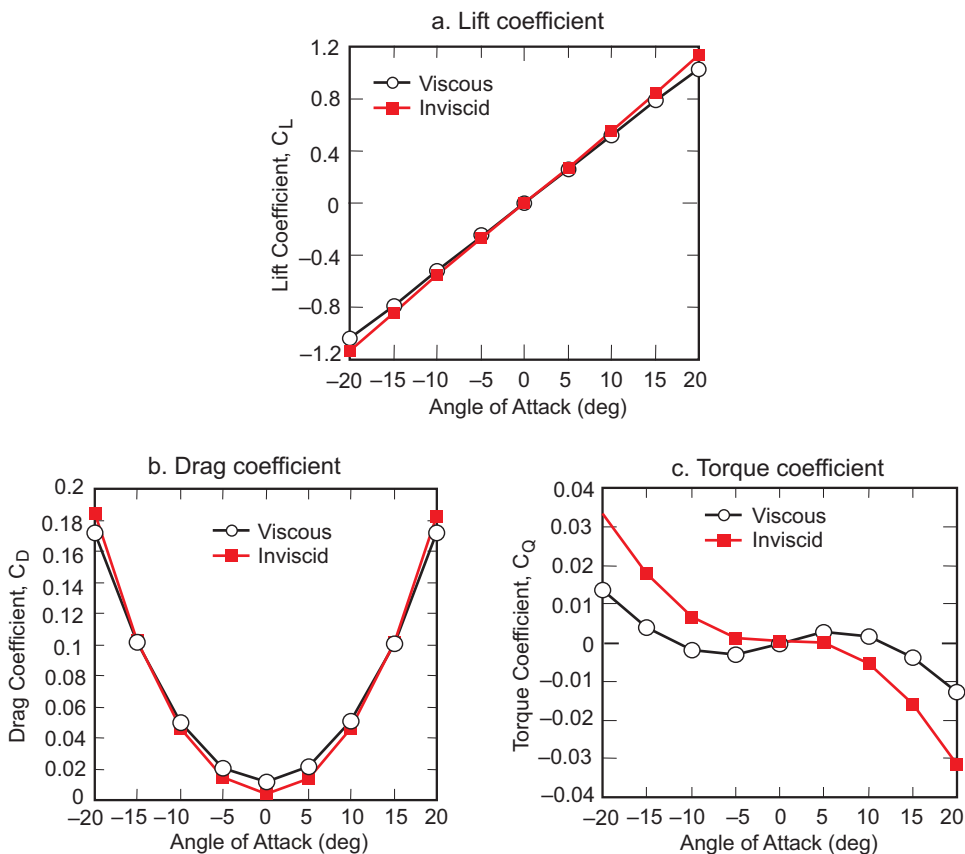


Figure 7. Effects of viscosity on lift, drag, and torque coefficients

doubled. A similar effect is shown for the drag and torque coefficients. In general, trailing-edge twist has the greatest effect on performance degradation. The graphs on the right show an average lift deficit of 3.6% and torque variation deficit of 1.3% from the ideal rudder. Therefore, the tightest tolerances should be maintained for the trailing-edge casting and its attachment to the rudder.

Spanwise Twist. Figure 10 presents the effects of spanwise twist on rudder lift, drag, and torque. Spanwise twist is shown to cause roughly a 2% to 3% deficit in lift coefficient, less than 1% variation in drag coefficient, and a negligible effect on torque coefficient. That deformation will not affect steering gear performance. Further investigation is required to fully understand the effect the variation in lift will have on overall ship maneuverability before tolerances can be relaxed.

Longitudinal Alignment of Foil Sections. Figure 11 presents the effects of longitudinal misalignment on rudder lift, drag, and torque. It was observed that, in this case, minor changes in modeling the geometry could significantly affect torque computations. Therefore, we took great care to ensure that the rudder models were perfectly symmetric. The forward deviation affects primarily the lift coefficient, whereas the aft deviation affects primarily the torque coefficient. However, the predicted results of longitudinal misalignment appear to be quite small. Therefore, tolerances for longitudinal alignment may be loosened.

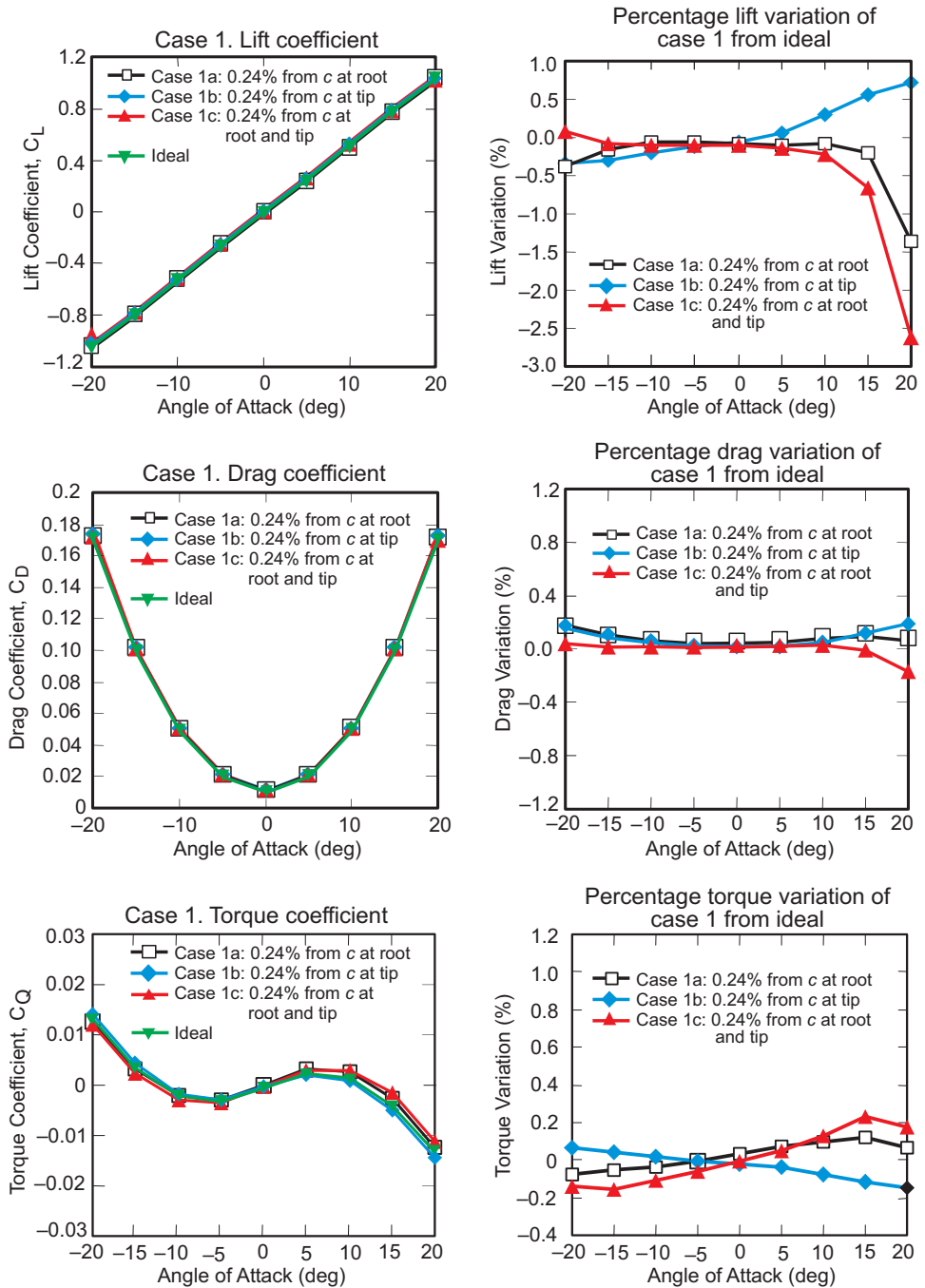


Figure 8. Effects of leading-edge droop on lift, drag, and torque coefficients (left) and percentage variations (right)

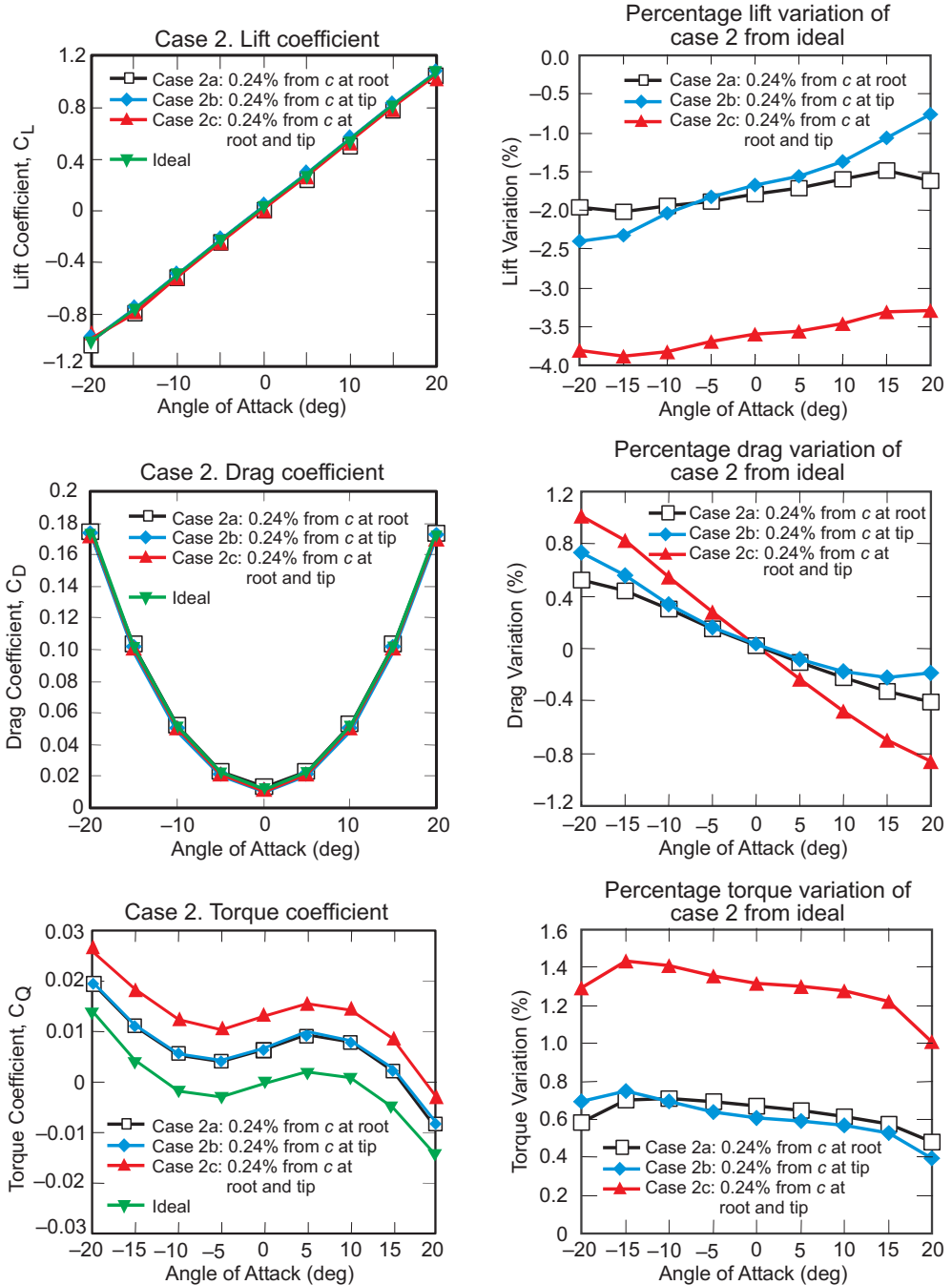


Figure 9. Effects of trailing-edge twist on lift, drag, and torque coefficients (left) and percentage variations (right)

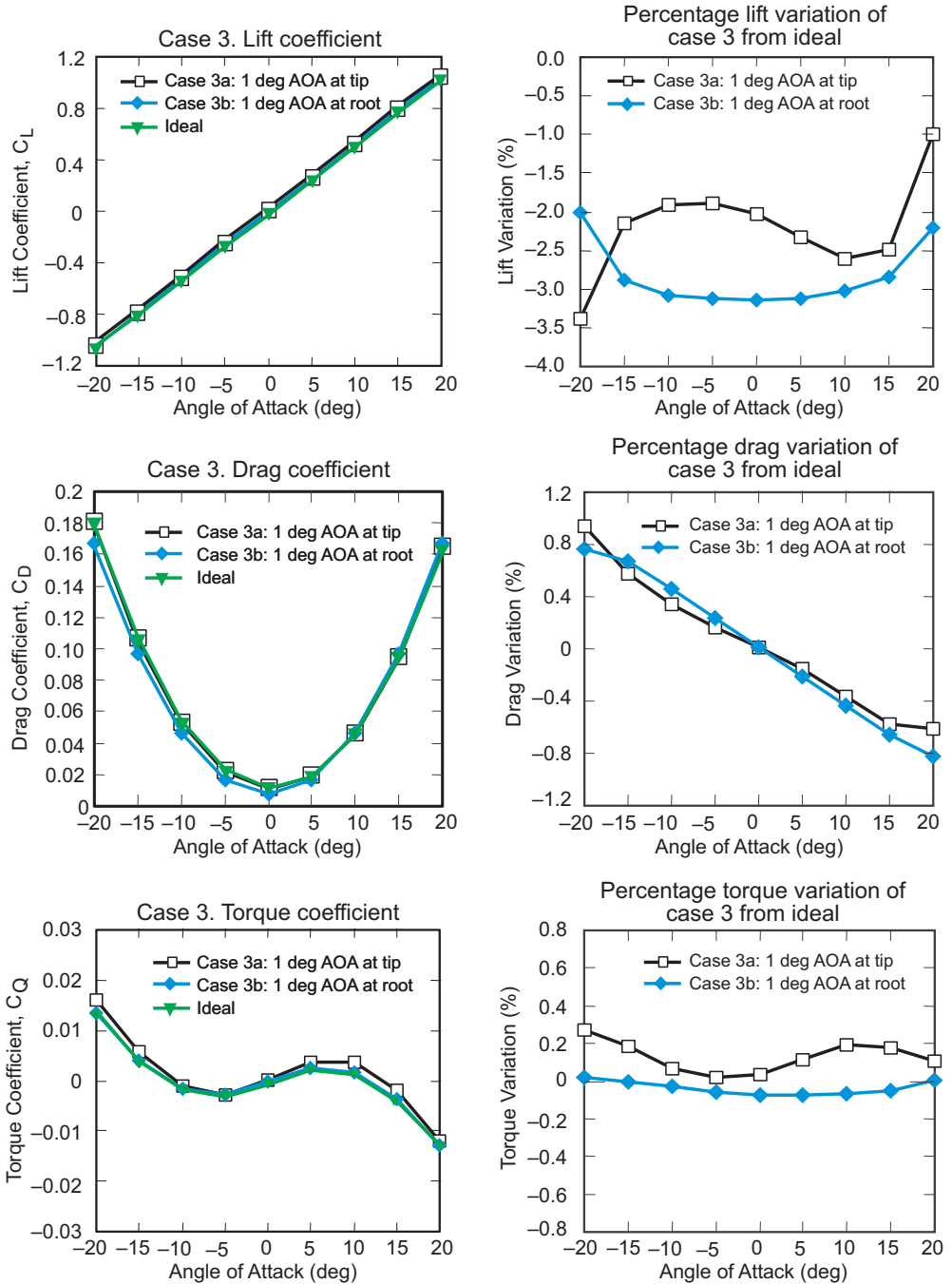


Figure 10. Effects of spanwise twist on lift, drag, and torque coefficients (left) and percentage variations (right)

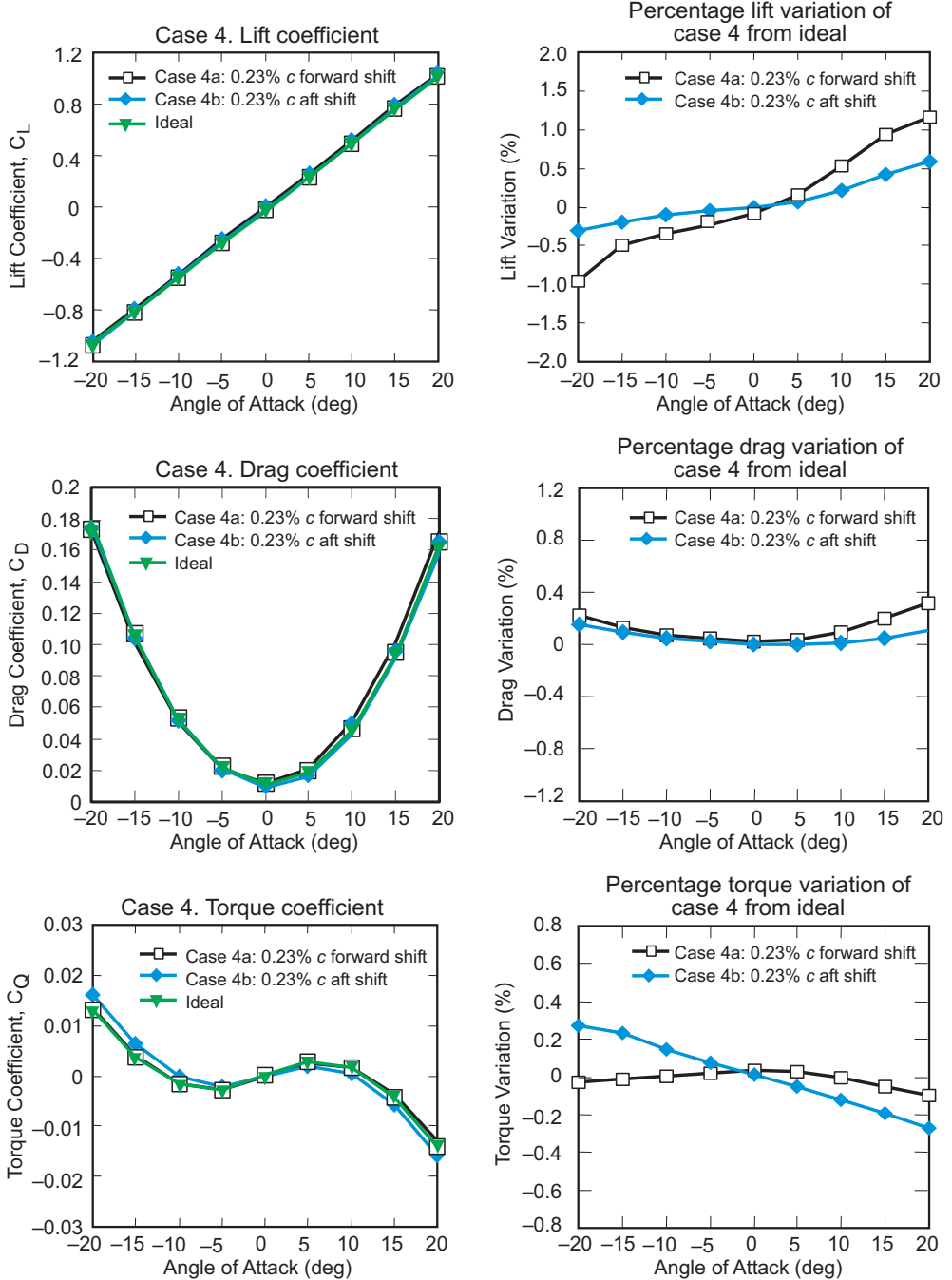


Figure 11. Effects of longitudinal misalignment on lift, drag, and torque coefficients (left) and percentage variations (right)

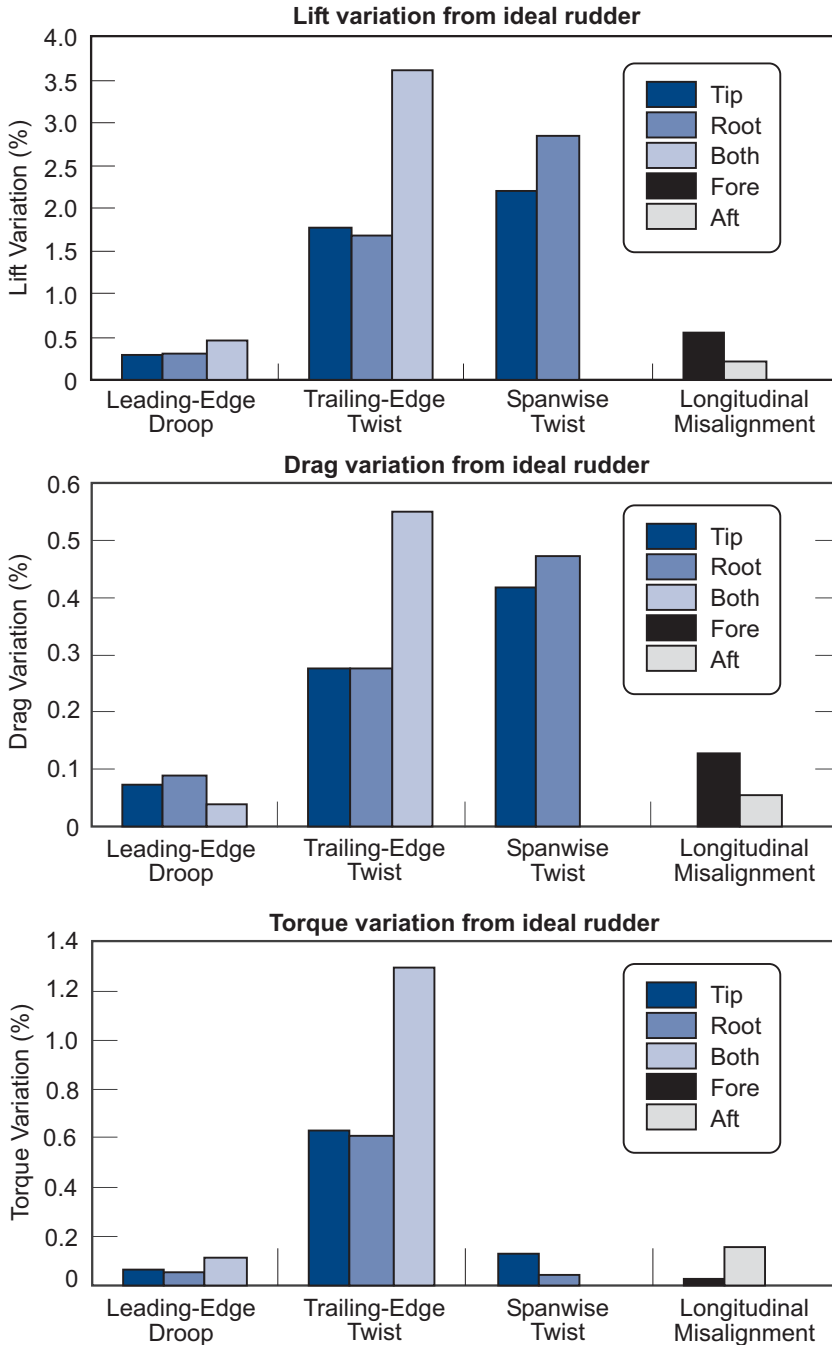


Figure 12. Rudder performance summary for lift (top), drag (middle), and torque (bottom)

Performance Variations. Figure 12 summarizes the results for each variation case. The variations were computed using the following equation:

$$\overline{\Delta C_X} = \frac{\sum_{i=1}^N |C_X^{\text{var}}(\alpha_i) - C_X^{\text{ideal}}(\alpha_i)|}{N}, \quad (20)$$

where N is the number of angles of attack (taken here to be nine), and X can be L , D , or Q , for lift, drag, or torque, respectively. The figure shows that trailing-edge twist (case 2) has the greatest effect on rudder performance.

Conclusions and Recommendations

The effects of manufacturing variations on rudder performance were investigated using an unstructured viscous computational fluid dynamics approach. Four major types of variations were studied: leading-edge droop, trailing-edge twist, spanwise twist, and longitudinal misalignment. For each variation case, solutions were generated for nine different angles of attack. The ideal, or nominal, rudder was also run at the same conditions. The resulting performance variations were then computed by comparing the deformed rudder case with the nominal design.

Of the three rudder performance parameters (lift, drag, and torque), torque was most affected by variations in rudder geometry. It is also the parameter that most affects the steering-gear performance.

The results showed clearly that trailing-edge twist (case 2) had the greatest effect on rudder performance. Additionally, spanwise twist (case 3) strongly influenced lift performance but had no effect on rudder torque; hence, the steering gear would not be affected. However, leading-edge droop (case 1) and longitudinal misalignment (case 4) were shown to have much smaller effects on rudder performance. Thus, the following recommendations are given:

- Existing tolerances should be maintained for trailing-edge twist.
- Tolerances for leading-edge droop (case 1) and longitudinal misalignment (case 4) may be loosened.

The steering gear effects associated with spanwise twist appear to be minimal; therefore, allowing larger spanwise twist holds promise. However, before construction tolerances are relaxed, additional work should be performed to understand the lift variation resulting from spanwise twist and the consequent effect on overall ship maneuverability. In addition, future work should investigate the effects of nonuniform inflow caused by the propeller and hull, as well as how the individual construction deviations investigated here combine to affect rudder performance.

References

1. Y.T. Shen, C.W. Jiang, and K.D. Remmers, "A Twisted Rudder for Reduced Cavitation," *J. Ship Research*, Vol. 41, No. 4, December 1997, pp. 260–272.
2. D.L. Marcum and N.P. Weatherill, "Unstructured Grid Generation Using Iterative Point Insertion and Local Reconnection," *AIAA J.*, Vol. 33, No. 9, September 1995, pp. 1619–1625.

3. D.L. Marcum, N.P. Weatherill, M.J. Marchant, and F. Beaven, "Generation of Unstructured Grids for Viscous Flow Applications," presented at 33rd AIAA Aerospace Sciences Meeting and Exhibit, Reno, Nev., January 9–12, 1995, AIAA Paper 95-0212, marcum@erc.msstate.edu.
4. D.L. Marcum, "Generation of High-Quality Unstructured Grids for Computational Field Simulation," presented at 6th International Symposium on Computational Fluid Dynamics, Lake Tahoe, Nev., September 1995, marcum@erc.msstate.edu.
5. D.L. Marcum, "Adaptive Unstructured Grid Generation for Viscous Flow Applications," *AIAA J.*, Vol. 34, No. 11, November 1996, pp. 2440–2443.
6. D.L. Marcum, "Control of Point Placement and Connectivity in Unstructured Grid Generation Procedures," presented at IX International Conference on Finite Elements in Fluids, Venice, Italy, October 15–21, 1995, marcum@erc.msstate.edu.
7. A.J. Chorin, "A Numerical Method for Solving Incompressible Viscous Flow Problems," *J. Comput. Phys.*, Vol. 2, No. 1, August 1967, pp. 12–26.
8. D. Pan and S.R. Chakravarthy, "Unified Formulation for Incompressible Flows," presented at 27th AIAA Aerospace Sciences Meeting and Exhibit, Reno, Nev., January 9–12, 1989, AIAA Paper 89-0122.
9. S.E. Rogers and D. Kwak, "Upwind Differencing for the Time-Accurate Incompressible Navier-Stokes Equations," *AIAA J.*, Vol. 28, No. 2, February 1990, pp. 253–262.
10. L.K. Taylor, "Unsteady Three-Dimensional Incompressible Algorithm Based on Artificial Compressibility," PhD dissertation, Mississippi State University, May 1991. (Available through Mississippi State University Library Interlibrary Loan.)
11. W.K. Anderson, R.D. Rausch, and D.L. Bonhaus, "Implicit/Multigrid Algorithms for Incompressible Turbulent Flows on Unstructured Grids," *J. Comput. Phys.*, Vol. 128, No. 2, October 1996, pp. 391–408.
12. T.J. Coakley, "Development of Turbulence Models for Aerodynamic Applications," presented at 28th AIAA Fluid Dynamics Conference and Exhibit, Snowmass Village, Colo., June 29–July 2, 1997, AIAA Paper 97-2009.
13. P. Spalart and S. Allmaras, "A One-Equation Turbulence Model for Aerodynamic Flows," presented at 30th AIAA Aerospace Sciences Meeting and Exhibit, Reno, Nev., January 6–9, 1992, AIAA Paper 92-0439.
14. P.L. Roe, "Approximate Riemann Solvers, Parameter Vector, and Difference Schemes," *J. Comput. Phys.*, Vol. 43, No. 2, October 1981, pp. 357–372.
15. D.L. Whitfield, *Newton-Relaxation Schemes for Nonlinear Hyperbolic Systems*, Engineering and Industrial Research Station Report MSSU-EIRS-ASE-90-3, Mississippi State University, Miss., October 1990. (Available through Mississippi State University Library Interlibrary Loan.)
16. J.M. Ortega and W.C. Rheinboldt, *Iterative Solution of Nonlinear Equations in Several Variables*, Academic Press, New York, 1970.
17. K.J. Vanden and D.L. Whitfield, "Direct and Iterative Algorithms for the Three-Dimensional Euler Equations," *AIAA J.*, Vol. 33, No. 5, May 1995, pp. 851–858.
18. D.L. Whitfield and L.K. Taylor, "Discretized Newton-Relaxation Solution of High Resolution Flux-Difference Split Schemes," *Proc. AIAA 10th Annual Computational Fluid Dynamics Conference*, 1991, pp. 134–145 (June 1991, AIAA Paper 91-1539).
19. E.F. Toro, *Riemann Solvers and Numerical Methods for Fluid Dynamics: A Practical Introduction*, 2d ed., Springer-Verlag, Berlin/Heidelberg, June 1999.
20. C. Sheng, L.K. Taylor, and D.L. Whitfield, "A Multigrid Algorithm for Unsteady Incompressible Euler and Navier-Stokes Flow Computations," presented at 6th

International Symposium on Computational Fluid Dynamics, Lake Tahoe, Nev., September 4–8, 1995.

21. W.H. Brewer, “On Simulating Tip-Leakage Vortex Flow to Study the Nature of Cavitation Inception,” PhD dissertation, Mississippi State University, May 2002, <http://library.msstate.edu/etd/show.asp?etd=etd-04102002-134949>.

Author Profiles



John P. Hackett is Chief Scientist and Director of Advanced Ship Design, Hydrodynamics, and Signatures at Northrop Grumman Ship Systems. His area of expertise is conceptual and preliminary ship design, as well as hydrodynamics. Dr. Hackett’s 30+ years of marine experience include service as chair of the School of Naval Architecture and Marine Engineering, University of New Orleans. He received Litton’s 1996 Charles B. Thornton Advanced Technology Achievement award for his work on hull form design and hydrodynamics. He holds two patents, with a third pending. Dr. Hackett is active in the Society of Naval Architects and Marine Engineers and has served as its vice president. His technical papers, focused on ship hydrodynamics and design, have appeared in *Ocean Engineering* and publications of the Society of Naval Architects and Marine Engineers, American Society of Naval Engineers, The Royal Institution of Naval Architects, Society of Automotive Engineers, and Office of Naval Research. He holds a BSE in naval architecture and marine engineering, MSE degrees in applied mechanics and in naval architecture and marine engineering, and a PhD in naval architecture and marine engineering, all from the University of Michigan.

john.hackett@ngc.com



Wesley H. Brewer is currently an adjunct professor at Mississippi State University and president of Fluid Physics International. Previously, he worked as a test engineer and operations team leader at the U.S. Navy’s William B. Morgan Large Cavitation Channel, where he performed experimental work on the Navy’s Virginia-class submarine. He was honored with two U.S. Navy awards for his work. His numerous technical papers have appeared in or are awaiting publication in such journals as *Journal of Ship Research*, *Journal of Fluids Engineering*, and *AIAA Journal*. Dr. Brewer holds a BS in engineering science and mechanics from the University of Tennessee, an MS in ocean engineering from the Massachusetts Institute of Technology, and a PhD in computational engineering from Mississippi State University.

wbrewer@fluidphysics.com